Volume 4 | Number 37 | 7 October 2016 | Pages 14035–14466

Journal of Materials Chemistry A

Materials for energy and sustainability

www.rsc.org/MaterialsA

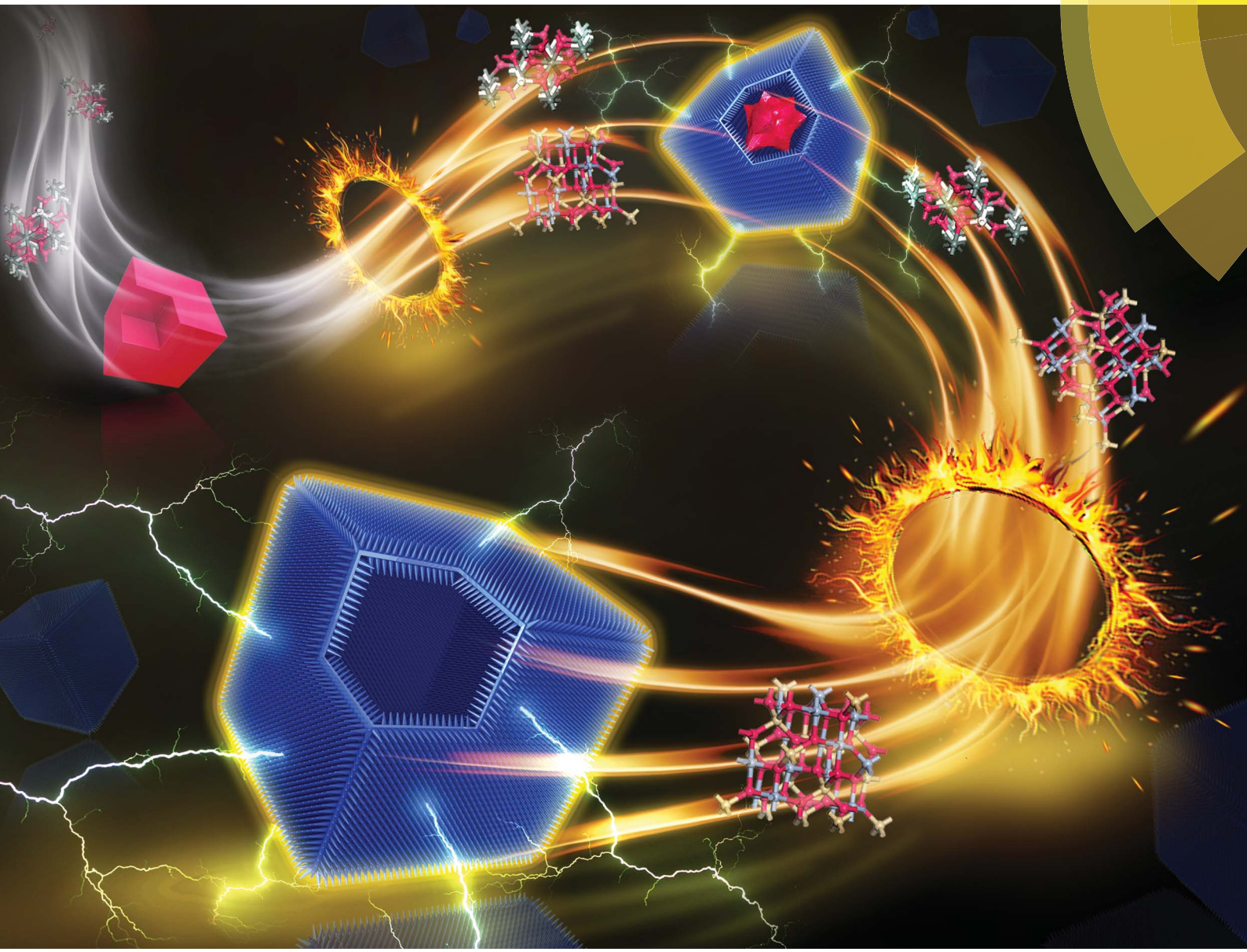

ISSN 2050-7488

ROYAL SOCIETY OF CHEMISTRY

COMMUNICATION

Liqiang Mai *et al.*

Gradient-temperature hydrothermal fabrication of hierarchical Zn_2SnO_4 hollow boxes stimulated by thermodynamic phase transformation

175 YEARS

Journal of Materials Chemistry A

COMMUNICATION

View Article Online
View Journal | View Issue

Cite this: J. Mater. Chem. A, 2016, 4, 14095

Received 16th July 2016
Accepted 17th August 2016

DOI: 10.1039/c6ta06016a

www.rsc.org/MaterialsA

Gradient-temperature hydrothermal fabrication of hierarchical Zn_2SnO_4 hollow boxes stimulated by thermodynamic phase transformation†

Xiong Liu,‡ Chaojiang Niu,‡ Jiashen Meng,‡ Xiaoming Xu, Xuanpeng Wang, Bo Wen, Ruiting Guo and Liqiang Mai*

We develop a facile gradient-temperature hydrothermal method to synthesize hierarchical Zn_2SnO_4 hollow boxes based on phase transformation between metastable $ZnSnO_3$ and stable Zn_2SnO_4. This strategy is widely extended to $ZnSnO_3$ microspheres, $ZnSn(OH)_6$ nanocubes and Co-ZIF-67 polyhedrons. When employed as a LIB anode, Zn_2SnO_4 hollow boxes exhibit apparently enhanced electrochemical performance.

Hollow micro-/nanostructures have attracted increasing attention due to their high reaction activity, good accessibility, superior mass transfer properties, well-defined cavities and chemical functionality.[1–8] Meanwhile, hierarchical structures, which are self-assembled with nano-building blocks, combine advantages of both nanomaterials and micromaterials.[9–13] In view of complexity and superior performance, hierarchical hollow structures have been explored in many intriguing applications such as energy storage, the catalytic field and so on.[5–9] For example, Lou and co-workers have reported a template-induced formation of CoSe@carbon nanocubes, which is based on the template-induced reaction between ZIF-67 nanocubes and Se powder at elevated temperature, and when applied as LIB anodes, the CoSe@carbon nanocubes show great lithium-storage performance.[6] Niu *et al.* have proposed a general strategy to synthesize complex nanotubes with different components and morphologies, which exhibit excellent electrochemical performance when used in lithium-ion batteries (LIBs) and sodium-ion batteries (SIBs) as well as supercapacitors.[8] The aforementioned research studies demonstrate the advantages of hollow structures.

Many efforts have been devoted to the controllable synthesis of hollow structures, especially for non-spherical hollow structures, with stress concentration and a stable framework.[5] Simultaneously, many kinds of synthetic methods have been adopted to construct hollow micro-/nanostructures, including chemical etching, templating, ion-exchange, Ostwald ripening and so on.[9–20] For instance, Yu and co-workers have reported a controlled hydrothermal synthesis of a new phase of $Co_3V_2O_8 \cdot nH_2O$ hollow hexagonal prismatic pencils, and the hollow hole is caused by orientated growth and preferential adsorption of NH_4^+.[14] Yin and co-workers have prepared TiO_2 hollow shells with controllable crystallinity and phases *via* a novel resin-protected calcination process.[16] All these hollow materials acquire a probative structure–activity relationship and allow for enhanced physicochemical properties. However, due to rare non-spherical templates, relatively high curvature radius on the edges and integrity of monolithic construction, the controllable fabrication of non-spherical hierarchical hollow structures with inorganic and/or organic component still remains a great challenge.

Herein, we develop a gradient-temperature hydrothermal method to synthesize hierarchical Zn_2SnO_4 hollow boxes. This method is based on the different reaction sequence of the precursors under relatively low- and high-temperature conditions, and the metastable $ZnSnO_3$ phase is changed into a stable Zn_2SnO_4 phase when temperature changes. The formation mechanism of hierarchical Zn_2SnO_4 hollow boxes, dissolution and recrystallization, has been specifically demonstrated. When employed as a LIB anode, the synthesized hierarchical Zn_2SnO_4 hollow boxes exhibit apparently improved electrochemical performance compared with non-hollow structures. Moreover, the synthetic method is widely extended to Zn_2SnO_4 hollow microspheres and Zn_2SnO_4 hollow nanoboxes as well as Co-ZIF hollow polyhedrons, indicating the good universality of this method.

As schematically shown in Fig. S1a,† representative experimental parameters like hydrothermal temperature and reaction time involved in previous reports are compendiously

State Key Laboratory of Advanced Technology for Materials Synthesis and Processing, Wuhan University of Technology, Wuhan 430070, China. E-mail: mlq518@whut.edu.cn

† Electronic supplementary information (ESI) available: Crystallographic parameters, schematic illustrations, size statistics, XRD patterns, EDS mapping, charge–discharge curves, SEM and TEM images and BET test results. See DOI: 10.1039/c6ta06016a

‡ These authors contributed equally to this work.

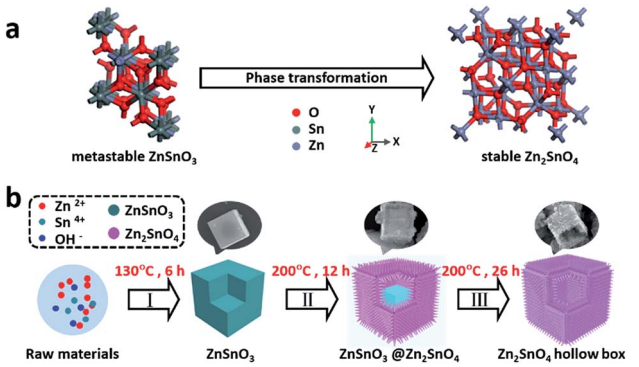

Fig. 1 (a) Crystal structure schematic diagrams and the phase transformation from $ZnSnO_3$ to Zn_2SnO_4. (b) Schematic illustrations of phase transformation and synthesis processes with morphology evolution under a gradient-temperature hydrothermal strategy.

summarized.[20–35] According to the synthetic conditions, it is found that the synthesis requirements of the Zn_2SnO_4 phase are stricter and harsher than those of the $ZnSnO_3$ phase. In other words, the metastable $ZnSnO_3$ phase tends to change into a stable Zn_2SnO_4 phase due to the thermodynamic driving force (Fig. 1a). The Zn_2SnO_4 phase has a cubic structure and the phase transformation of this specific crystal structure experiences a huge change of lattice parameters (Table S1†).

We successfully synthesized Zn_2SnO_4 hollow boxes based on a gradient-temperature hydrothermal method. As shown in the schematic diagram (Fig. 1b), metastable $ZnSnO_3$ solid microcubes formed at a relatively low temperature of 130 °C (step I). Then the structural transformation from the $ZnSnO_3$ phase to the Zn_2SnO_4 phase takes place at an uninterrupted high temperature of 200 °C, and $ZnSnO_3$ dissolves and recrystallizes. $ZnSnO_3$@Zn_2SnO_4 yolk–shelled microcubes are obtained at 200 °C *via* a heterogeneous nucleation process (step II). Finally, hierarchical Zn_2SnO_4 hollow boxes form along with the complete dissolution of interiors (step III). In detail, the $ZnSnO_3$ solid microcubes were preferentially formed at 130 °C after 6 h with the driving force from the concentration and reaction temperature in the hydrothermal processes. Then when the temperature was changed to 200 °C, the phase transformation happened and $ZnSnO_3$ microcubes gradually dissolved and then recrystallized due to thermodynamical factors. When the reaction was proceeded for 3 h, the Zn_2SnO_4 nanorods formed on its surface *via* a heterogeneous nucleation process (Fig. S2a and b†). When the reaction was proceeded for 6 and 8 h, the nanorods gradually assembled into a shell along with the dissolution of the inside, a void formed and the shell was separated from inner materials (Fig. S2c and d†). When the reaction was prolonged for 12, 16 and 26 h, respectively, the trend of the void between the internal and external components gradually increased, and a hollow structure with rod-like subunits was obtained in the end, with the pure Zn_2SnO_4 phase (Fig. 2f–h). This dissolution–recrystallization process is clearly depicted by *ex situ* SEM (Fig. 2a–d), and the corresponding TEM (Fig. 2e–h) and XRD (Fig. 2i–l). And the selected high resolution TEM of the external shell of the $ZnSnO_3$@Zn_2SnO_4 yolk–shelled microcube in Fig. 2a is indexed to the Zn_2SnO_4 phase, with a marked interplanar *d* spacing of 0.503 nm corresponding to

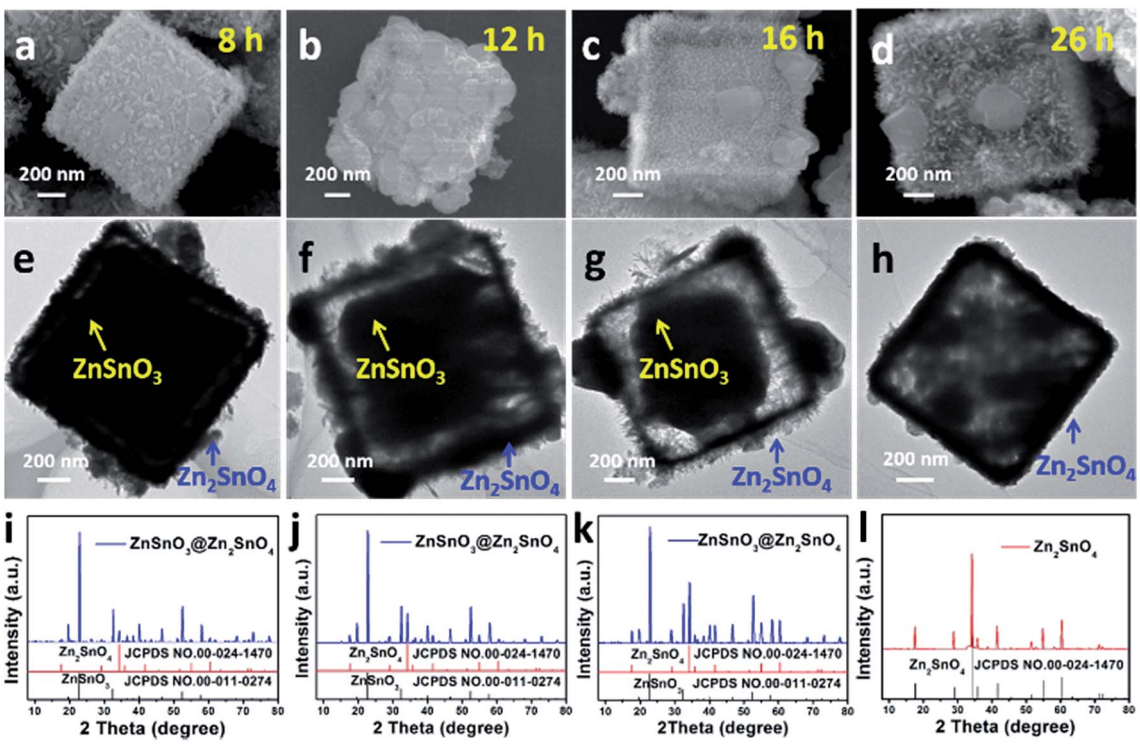

Fig. 2 SEM images of products prepared at 200 °C for 8 h (a), 12 h (b), 16 h (c), 26 h (d), the corresponding TEM images (e–h) and XRD pattern (i–l), respectively. Noting that all samples have gone through hydrothermal treatment at 130 °C for 6 h before reacting at 200 °C.

(111) lattice planes (Fig. S3†), proving the recrystallization process. In addition, when $ZnSnO_3$ microcubes were dispersed in deionized water and reacted at 200 °C, the yolk-shelled and hollow structures can also form, as seen in the SEM images (Fig. S4b and c†). By *ex situ* semi-quantitative element analysis with EDS technology (Fig. S5, Table S2†), the molar ratios of Zn to Sn elements roughly increase from 1.0 to 2.0, indicating the phase transformation from $ZnSnO_3$ to Zn_2SnO_4. All these results indicate the dissolution and phase transformation processes. A new interface emerged on the surface of the inner core during the dissolution process, but it presented a dynamic and ever-changing interface as well as the existence of the ion diffusion factor, all these elements were likely to prompt the heterogeneous nucleation on the shell interface. Especially, these possible guesses have also happened in other reports.[11–14]

Uniform $ZnSnO_3$ microcubes were obtained under relatively low-temperature conditions of 130 °C. Typical scanning electron microscopy (SEM) images depicted that the uniform $ZnSnO_3$ microcubes had side lengths of ~1 μm with a smooth surface (Fig. 3a and b). And all the diffraction peaks match well with those of standard XRD patterns of $ZnSnO_3$ (JCPDS no. 00-011-0274) (Fig. 3c). When under gradient-temperature hydrothermal conditions, in other words, the raw reagents went through relatively low- and high-temperature hydrothermal conditions during the sequential operating procedure, hierarchical Zn_2SnO_4 hollow boxes were obtained (JCPDS no. 00-024-1470) (Fig. 3d and e). These Zn_2SnO_4 hollow boxes are assembled with nanorods with ~100 nm length. Based on the statistical data (Fig. S6a and 6b†), the average sizes of hollow boxes range from 1.0 to 1.4 μm, demonstrating well-fabricated structures. This value is larger than that of the solid one due to heterogeneous nucleation on the solid surface. Meanwhile, from EDS elemental mapping (Fig. 3f), the uniform partial distributions of the Zn, Sn and O elements were depicted. Furthermore, the physical size and overall geometry of Zn_2SnO_4 hollow boxes had changed a little after extending the reaction time to 36 h, indicating the substantially endless growth processes (Fig. S7†), and the partially battered boxes exhibited the hollow characteristic as well.

In order to explore the main factors of driving force of dissolution, we individually developed the alkali corrosion test (Fig. S8 and S9†). The $ZnSnO_3$ microcubes are fretted and dissolved, and the XRD patterns match well with the pure $ZnSnO_3$ phase. It indicates that phase transformation does not happen during alkali corrosion. The phase transformation also happens when $ZnSnO_3$ microcubes are calcined at different temperatures in air (Fig. S10†). However, the transformation temperature is quirky and high and the new phase can be undetected even up to 200 °C, indicating that it is a dissolution–recrystallization process rather than a solid-to-solid process in the previous gradient-temperature hydrothermal experiments.

In our strategy, temperature plays an important role in the uniform construction of the as-prepared products. The phase transformation does not happen when the temperature is below 200 °C (Fig. S11†). When the high temperature changed from 200 °C to 220 °C (Scheme S1a†), the hollow structure cannot be obtained. Zn_2SnO_4 microflowers are composed of aggregative or assembled nanosheets with an irregular size of ~150 nm. The mixed geometrical morphologies are found in the intermediate products with a reduced reaction time (Fig. S12†). The molar ratios of Zn to Sn were ~1 and ~2 *via* an EDS elemental semi-quantitative analysis, respectively. So the mixed yolk–shelled and flower-like structures are the $ZnSnO_3$ phase and the Zn_2SnO_4 phase, respectively. These results were also proved by the selected area EDS elemental mapping and XRD patterns. The obtained yolk–shelled structure can deeply demonstrate the dissolution phenomenon of $ZnSnO_3$ microcubes (Fig. S12d†). The disordered Zn_2SnO_4 microflowers can be attributed to homogeneous nucleation and growth, because the excessively high temperature of 220 °C is not suitable for heterogeneous nucleation. Meanwhile, it does not mean that homogeneous nucleation does not happen at 200 °C, but that heterogeneous nucleation tends to be preferred with existence of $ZnSnO_3$ sites. Importantly, Zn_2SnO_4 nanosheets will form while pristine reagents just went through 200 °C under a simplex hydrothermal strategy, as shown in Fig. S13 and Scheme S1b,† from which it could be inferred that no heterogeneous nucleation sites and straightway homogeneous nucleation were observed. The nanosheets are loose-packed with a size of ~500 nm and a thickness of ~100 nm.

The specific surface area, *t*-plot curves and pore size distribution of $ZnSnO_3$ solid microcubes, $ZnSnO_3$@Zn_2SnO_4 yolk–shelled microcubes, Zn_2SnO_4 hollow boxes and Zn_2SnO_4 nanosheets were measured (Fig. S14†). Meanwhile, the relative data are summarized in Table S3.† It is noteworthy that the uniform porous type materials of Zn_2SnO_4 hollow boxes are shown in Fig. S14g–i,† with a mesoporous size of about 5 nm, and the formation of the numerous pores is attributed to the accumulation of uniform nanorods. The hollow structure is bound to possess the largest BET value of all samples, indicating its good Li-storage properties.

To confirm the universality of this gradient-temperature hydrothermal method, representative experimental parameters are also compendiously summarized (Fig. S1b†).[36–41] According to our synthetic strategy, different kinds of inorganic materials and metal–organic frameworks were also fabricated (Fig. 4). In detail, we prepared Zn_2SnO_4 hollow microspheres from $ZnSnO_3$ solid microspheres and Zn_2SnO_4 hollow nanoboxes from

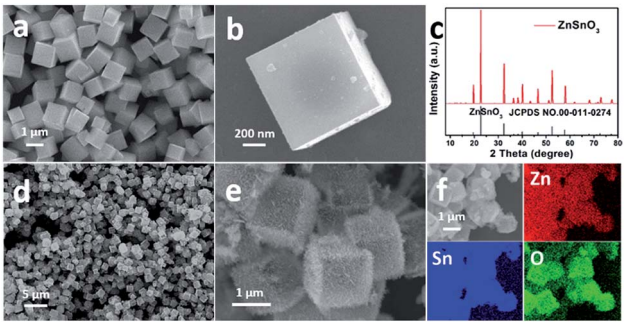

Fig. 3 SEM images (a and b) and the XRD pattern (c) of $ZnSnO_3$ microcubes. SEM images (d and e) and EDS elemental mapping (f) of Zn_2SnO_4 hollow boxes.

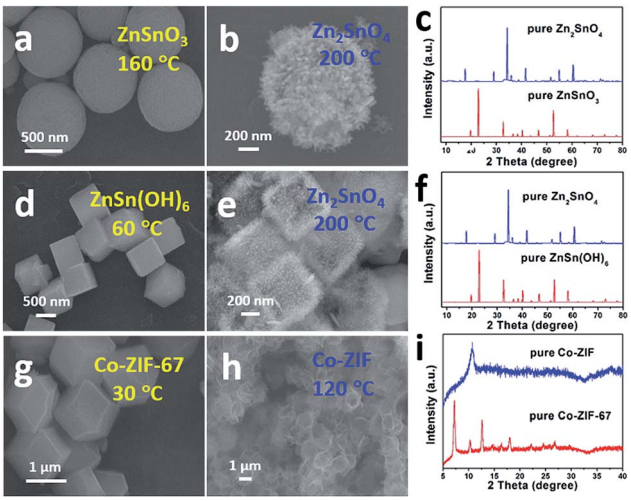

Fig. 4 Extensions of the gradient-temperature hydrothermal method. The sequential structural transformation from solid to hollow structures. (a–c) SEM images of $ZnSnO_3$ solid microspheres (a), Zn_2SnO_4 hollow microsphere (b), and their XRD patterns (c). (d–f) SEM images of $ZnSn(OH)_6$ solid nanocubes (d), Zn_2SnO_4 hollow nanoboxes (e), and their XRD patterns (f). (g–i) SEM images of Co-ZIF-67 solid polyhedrons (g), Co-ZIF hollow polyhedrons (h), and their XRD patterns (i).

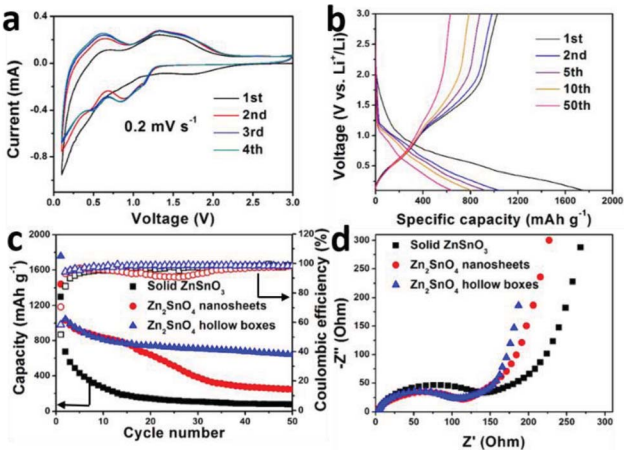

Fig. 5 Electrochemical tests. (a) Cyclic voltammograms for the first four cycles of Zn_2SnO_4 hollow boxes at a scanning rate of 0.2 mV s^{-1} in the potential range of 0.1–3.0 V. (b) Charge–discharge curves of Zn_2SnO_4 hollow boxes. (c) Cycling performances of Zn_2SnO_4 hollow boxes, Zn_2SnO_4 nanosheets and $ZnSnO_3$ solid microcubes at 200 mA g^{-1} *vs.* Li^+/Li in the potential range of 0.1–3.0 V. (d) Contrast of impedance investigations among Zn_2SnO_4 hollow boxes, Zn_2SnO_4 nanosheets and $ZnSnO_3$ solid microcubes at an open-circuit potential before cycling.

$ZnSn(OH)_6$ solid nanocubes as well as Co-ZIF hollow polyhedrons from Co-ZIF-67 solid polyhedrons. The XRD patterns clearly demonstrate the magical phase transformation (Fig. 4c, f and i). Meanwhile, according to the rational size distribution statistics with 30 representative individuals (Fig. S6c–h†), the increased sizes, typically ~200 nm, are estimated by comparing solid and hollow samples. All results mentioned above elucidate that our method has great universality and the method prolongs the strategy to construct hollow structures and extends the properties of bulk materials.

When employed as a LIB anode, electrochemical measurements of Zn_2SnO_4 hollow boxes were performed. The cyclic voltammetry (CV) curves of Zn_2SnO_4 hollow boxes (Fig. 5a) were obtained at 0.2 mV s^{-1} in the range from 0.1 to 3.0 V *vs.* Li^+/Li. The last three cycles are almost overlapped and this result reveals good electrochemical redox reaction reversibility. However, these three curves differ from the first curve just during the cathodic scan, signifying the irreversible phase change of the Zn_2SnO_4 structure, in agreement with previous reports.[22,25]

Meanwhile, the Zn_2SnO_4 hollow boxes afford the best results in terms of the cycling stability and reversible capacity value compared with that of pristine $ZnSnO_3$ solid microcubes and Zn_2SnO_4 nanosheets. When all the materials are tested at a current density of 200 mA g^{-1}, the discharge capacities of $ZnSnO_3$ solid microcubes (Fig. S15b†), Zn_2SnO_4 nanosheets (Fig. S15a†) and Zn_2SnO_4 hollow boxes (Fig. 5b) are obtained as 78.3, 247.0 and 641.8 mA h g^{-1}, after 50 cycles, respectively. And the capacity retention of Zn_2SnO_4 hollow boxes is higher than that of $ZnSnO_3$ solid microcubes and Zn_2SnO_4 nanosheets. Moreover, the Zn_2SnO_4 hollow boxes have slight capacity fading during the whole process. The improved cyclability benefits from hierarchical hollow structures and nanoscale nanorods. This structure provides more interspace to buffer volume expansion, shortens ion diffusion paths and ensures an appropriate contact area between the electrodes and electrolyte. However, the $ZnSnO_3$ solid microcubes encounter violent capacity fading during entire cycles due to bulk and solid features without the ability to accommodate the huge volume change. The Zn_2SnO_4 nanosheets show two stages of slight capacity fading rate during the early 20 cycles, but it becomes a sharp decline in the subsequent cycles. The first stable stage is attributed to the size of the nanometer level of Zn_2SnO_4 nanosheets. But aggregation and pulverization of nanosheets in the next stage lead to fast capacity decline. The superior rate performance and long-life cycling performance also demonstrate the advantage of the hollow structure (Fig. S16 and S17†). The Zn_2SnO_4 hollow boxes recover 78.1% of their initial capacity after being tested at various rates of 100, 200, 500, 1000 and again at 100 mA g^{-1}, which is higher than that of Zn_2SnO_4 nanosheets (48.4%) and $ZnSnO_3$ solid microcubes (29.5%) (Fig. S16†). When tested at 200 mA g^{-1} for long cycles, the Zn_2SnO_4 hollow boxes exhibited 389 mA h g^{-1} after 200 cycles, which is higher than the theoretical capacity of commercial graphite (Fig. S17†). Because of solid features of the internal structure, the yolk–shell structure does not exhibit good performance as that of the hollow one during the lithium intercalation/deintercalation processes.

Electrochemical impedance spectroscopy (EIS) measurements were carried out (Fig. 5d). The charge transfer resistances (R_{ct}) of electrodes based on Zn_2SnO_4 hollow boxes, Zn_2SnO_4 nanosheets and $ZnSnO_3$ solid microcubes are 104, 121 and 150 Ω, respectively. And the slope of the curve in the low frequency area of Zn_2SnO_4 hollow boxes is largest. These results

suggest that the fast electronic mobility of Zn_2SnO_4 hollow boxes is conducive to their electrochemical performance.[42–47] The SEM images of Zn_2SnO_4 hollow boxes, Zn_2SnO_4 nanosheets and $ZnSnO_3$ solid microcubes after 30 cycles are shown in Fig. S18.† The Zn_2SnO_4 hollow boxes possess an integrated cubic morphology; however, the Zn_2SnO_4 nanosheets and $ZnSnO_3$ solid microcubes are both agglutinate and cracked. Compared to previously reported $ZnSnO_3$ or Zn_2SnO_4 materials (Table S4†), the above results demonstrate that our constructed structures possess comparable performance in terms of capacity as well as cycle life.

Conclusions

We report a gradient-temperature hydrothermal method to construct hierarchical Zn_2SnO_4 hollow boxes. The obtained results are based on phase transformation between metastable $ZnSnO_3$ and stable Zn_2SnO_4. And the formation mechanism of hierarchical Zn_2SnO_4 hollow boxes, and their dissolution and recrystallization have been demonstrated in detail. In addition, the increased size before and after the phase transformation is related to the geometrical size of stable-phase materials, which is ascribed to heterogeneous nucleation on the solid surface. This general strategy is effectively extended to hollow structures based on $ZnSnO_3$ microspheres, $ZnSn(OH)_6$ nanocubes and Co-ZIF-67 polyhedrons. When employed as a LIB anode, hierarchical Zn_2SnO_4 hollow boxes exhibit apparently improved electrochemical performance compared with non-hollow structures. Therefore, this gradient-temperature hydrothermal method based on phase transformation opens a novel door to the fabrication of hierarchical hollow nanostructures, which can also be potentially extended to other systems and frontier fields.

Acknowledgements

This work was supported by the National Key Research Program of China (2016YFA0202603), the National Basic Research Program of China (2013CB934103), the National Natural Science Foundation of China (51521001, 51272197, 51302203), the National Natural Science Fund for Distinguished Young Scholars (51425204), the Hubei Provincial Natural Science Fund for Distinguished Young Scholars (2014CFA035), and the Fundamental Research Funds for the Central Universities (WUT: 2016III004 and 2016III006) and the Students Innovation and Entrepreneurship Training Program (2015-CL-B1-23 and 2016-CL-A1-40). We thank Prof. D. Y. Zhao of Fudan University for useful discussions and assistance with the manuscript.

Notes and references

1 J. Y. Wang, H. J. Tang, L. J. Zhang, H. Ren, R. B. Yu, Q. Jin, J. Qi, D. Mao, M. Yang, Y. Wang, P. R. Liu, Y. Zhang, Y. R. Wen, L. Gu, G. H. Ma, Z. G. Su, Z. Y. Tang, H. J. Zhao and D. Wang, *Nature Energy*, 2016, **1**, 16050.
2 Z. M. Liu, X. Y. Yu and U. Paik, *Adv. Energy Mater.*, 2016, **6**, 1502318.
3 X. Y. Yu, L. Yu and X. W. Lou, *Adv. Energy Mater.*, 2016, **6**, 1501333.
4 L. F. Shen, L. Yu, X. Y. Yu, X. G. Zhang and X. W. Lou, *Angew. Chem., Int. Ed.*, 2015, **54**, 1868–1872.
5 Q. L. Wei, S. S. Tan, X. Y. Liu, M. Y. Yan, F. C. Wang, Q. D. Li, Q. Y. An, R. M. Sun, K. N. Zhao, H. G. Wu and L. Q. Mai, *Adv. Funct. Mater.*, 2015, **25**, 1773–1779.
6 H. Hu, J. T. Zhang, B. Y. Guan and X. W. Lou, *Angew. Chem., Int. Ed.*, 2016, **55**, 9514–9518.
7 J. Qi, X. Y. Lai, J. Y. Wang, H. J. Tang, H. Ren, Y. Yang, Q. Jin, L. J. Zhang, R. B. Yu, G. H. Ma, Z. G. Su, H. J. Zhao and D. Wang, *Chem. Soc. Rev.*, 2015, **44**, 6749–6773.
8 C. J. Niu, J. S. Meng, X. P. Wang, C. H. Han, M. Y. Yan, K. N. Zhao, X. M. Xu, W. H. Ren, Y. L. Zhao, L. Xu, Q. J. Zhang, D. Y. Zhao and L. Q. Mai, *Nat. Commun.*, 2015, **6**, 7402.
9 L. Q. Mai, X. C. Tian, X. Xu, L. Chang and L. Xu, *Chem. Rev.*, 2014, **114**, 11828–11862.
10 D. W. Su, S. X. Dou and G. X. Wang, *J. Mater. Chem. A*, 2014, **2**, 11185–11194.
11 L. L. Wang, W. Q. Zhang, C. H. Wang, D. Wang, Z. P. Liu, Q. Y. Hao, Y. Wang, K. B. Tang and Y. T. Qian, *J. Mater. Chem. A*, 2014, **2**, 4970–4974.
12 D. L. Wang, Y. C. Yu, H. He, J. Wang, W. D. Zhou and H. D. Abruna, *ACS Nano*, 2015, **9**, 1775–1781.
13 J. Liu, C. Wu, D. D. Xiao, P. Kopold, L. Gu, P. A. V. Aken, J. Maier and Y. Yu, *Small*, 2016, **12**, 2354.
14 F. F. Wu, S. L. Xiong, Y. T. Qian and S. H. Yu, *Angew. Chem., Int. Ed.*, 2015, **54**, 10787–10791.
15 X. J. Zhu, Z. P. Guo, P. Zhang, G. D. Du, R. Zeng, Z. X. Chen, S. Li and H. K. Liu, *J. Mater. Chem.*, 2009, **19**, 8360–8365.
16 H. Y. Liu, J. B. Joo, M. Dahl, L. S. Fu, Z. Z. Zeng and Y. D. Yin, *Energy Environ. Sci.*, 2015, **8**, 286–329.
17 Z. C. Zhang, Y. F. Chen, S. He, J. C. Zhang, X. B. Xu, Y. Yang, F. Nosheen, F. Saleem, W. He and X. Wang, *Angew. Chem., Int. Ed.*, 2014, **126**, 12725–12729.
18 J. S. Meng, Z. A. Liu, C. J. Niu, X. M. Xu, X. Liu, G. B. Zhang, X. P. Wang, M. Huang, Y. Yu and L. Q. Mai, *J. Mater. Chem. A*, 2016, **4**, 4893–4899.
19 Z. L. Jian, P. Liu, F. J. Li, M. W. Chen and H. S. Zhou, *J. Mater. Chem. A*, 2014, **2**, 13805–13809.
20 Y. W. Wang, J. T. He, C. C. Liu, W. H. Chong and H. Y. Chen, *Angew. Chem., Int. Ed.*, 2015, **54**, 2022–2051.
21 S. Yuvaraj, W. J. Lee, C. W. Lee and R. K. Selvan, *RSC Adv.*, 2015, **5**, 67210–67219.
22 Y. J. Chen, B. H. Qu, L. Mei, D. N. Lei, L. B. Chen, Q. H. Li and T. H. Wang, *J. Mater. Chem.*, 2012, **22**, 25373–25379.
23 Y. Zhao, Y. Huang, X. Sun, H. J. Huang, K. Wang, M. Zong and Q. F. Wang, *Electrochim. Acta*, 2014, **120**, 128–132.
24 K. Kim, A. Annamalai, S. H. Park, T. H. Kwon, M. W. Pyeon and M. J. Lee, *Electrochim. Acta*, 2012, **76**, 192–200.
25 W. T. Song, J. Xie, W. Y. Hu, S. Y. Liu, G. S. Cao, T. J. Zhu and X. B. Zhao, *J. Power Sources*, 2013, **229**, 6–11.
26 C. T. Cherian, M. R. Zheng, M. V. Reddy, B. V. R. Chowdari and C. H. Sow, *ACS Appl. Mater. Interfaces*, 2013, **5**, 6054–6060.

27 X. F. Chen, Y. Huang, H. J. Huang, M. Y. Wang and K. Wang, *Mater. Lett.*, 2015, **149**, 33–36.
28 Q. S. Xie, Y. T. Ma, X. Q. Zhang, H. Z. Guo, A. L. Lu, L. S. Wang, G. H. Yue and D. L. Peng, *Electrochim. Acta*, 2014, **141**, 374–383.
29 Y. Zhao, L. F. Hu, H. Liu, M. Y. Liao, X. S. Fang and L. M. Wu, *Sci. Rep.*, 2014, **4**, 6847.
30 Z. D. Li, Y. Zhou, J. Y. Zhang, W. G. Tu, Q. Liu, T. Yu and Z. G. Zou, *Cryst. Growth Des.*, 2012, **12**, 1476–1481.
31 M. A. Alpuche-Aviles and Y. Y. Wu, *J. Am. Chem. Soc.*, 2009, **131**, 3216–3224.
32 K. Y. Lee, D. Kim, J. H. Lee, T. Y. Kim, M. K. Gupta and S. W. Kim, *Adv. Funct. Mater.*, 2014, **24**, 37–43.
33 G. X. Ma, R. J. Zou, L. Jiang, Z. Y. Zhang, Y. F. Xue, L. Yu, G. S. Song, W. Y. Li and J. Q. Hu, *CrystEngComm*, 2012, **14**, 2172–2179.
34 E. L. Foletto, S. L. Jahn and R. F. P. M. Moreira, *J. Appl. Electrochem.*, 2010, **40**, 59–63.
35 J. Zeng, M. D. Xin, K. W. Li, H. Wang, H. Yan and W. J. Zhang, *J. Phys. Chem. C*, 2008, **112**, 4159–4167.
36 B. Y. Geng, C. H. Fang, F. M. Zhan and N. Yu, *Small*, 2008, **4**, 1337–1343.
37 J. Z. Yin, F. Gao, C. Z. Wei and Q. Y. Lu, *Inorg. Chem.*, 2012, **51**, 10990–10995.
38 L. X. Han, J. Liu, Z. J. Wang, K. Zhang, H. Luo, B. Xu, X. Zou, X. Zheng, B. Ye and X. B. Yu, *CrystEngComm*, 2012, **14**, 3380–3386.
39 L. L. Wang, K. B. Tang, Z. P. Liu, D. Wang, J. Sheng and W. Cheng, *J. Mater. Chem.*, 2011, **21**, 4352–4357.
40 W. W. Zhan, Q. Kuang, J. Z. Zhou, X. J. Kong, Z. X. Xie and L. S. Zheng, *J. Am. Chem. Soc.*, 2013, **135**, 1926–1933.
41 J. Yang, F. J. Zhang, H. Y. Lu, X. Hong, H. L. Jiang, Y. Wu and Y. D. Li, *Angew. Chem., Int. Ed.*, 2015, **54**, 10889–10893.
42 H. Hu, L. Han, M. Z. Yu, Z. Y. Wang and X. W. Lou, *Energy Environ. Sci.*, 2016, **9**, 107–111.
43 X. P. Wang, C. J. Niu, J. S. Meng, P. Hu, X. M. Xu, X. J. Wei, L. Zhou, K. N. Zhao, W. Luo, M. Y. Yan and L. Q. Mai, *Adv. Energy Mater.*, 2015, **5**, 1500716.
44 C. J. Niu, J. S. Meng, C. H. Han, K. N. Zhao, M. Y. Yan and L. Q. Mai, *Nano Lett.*, 2014, **14**, 2873–2878.
45 W. W. Deng, J. F. Qian, Y. L. Cao, X. P. Ai and H. X. Yang, *Small*, 2016, **5**, 583–587.
46 Y. Zhao, X. F. Li, B. Yan, D. J. Li, S. Lawes and X. L. Sun, *J. Power Sources*, 2015, **274**, 869–884.
47 Y. Zhao, X. F. Li, B. Yan, D. B. Xiong, D. J. Li, S. Lawes and X. L. Sun, *Adv. Energy Mater.*, 2016, **6**, 1502175.

